





# A Multi-modal Deformable Land-air Robot for Complex Environments

Xinyu Zhang<sup>1</sup> , Yuanhao Huang<sup>1,2</sup> , Kangyao Huang<sup>3</sup> , Xiaoyu Wang<sup>1</sup>, Dafeng Jin<sup>1,4</sup>,  
Huaping Liu<sup>3</sup>  and Jun Li<sup>1</sup>

**Abstract**—Single locomotion robots often struggle to adapt in highly variable or uncertain environments, especially in emergencies. In this paper, a multi-modal deformable robot is introduced that can both fly and drive. Compatibility issues with multi-modal locomotive fusion for this hybrid land-air robot are solved using proposed design conceptions, including power settings, energy selection, and designs of deformable structure. The robot can also automatically transform between land and air modes during 3D planning and tracking. Meanwhile, we proposed a algorithms for evaluation the performance of land-air robots. A series of comparisons and experiments were conducted to demonstrate the robustness and reliability of the proposed structure in complex field environments.

## I. INTRODUCTION

Field tasks such as post-disaster mapping, situational awareness and analysis, search and rescue, and even special operations typically require robots that can move and work in uncertain and complex environments. However, it is often difficult for conventional single locomotion robots to adapt in these conditions. In contrast, multi-modal robots exhibit much higher flexibility and adaptability by combining wheels, legs, propellers, wings, fins, and hybrid actuators to achieve motion [1]. For example, land-air robots [2]–[6] offer both flying and driving capabilities for increased spatial flexibility while reducing the energy demands of continuous flight.

Similarly, hybrid vehicles with rotary wings have shown potential for seamless and dynamic switching between modalities [7]. Many of these systems are comprised of a quad-rotor hinged at the center of a cylindrical cage or a pair of coaxial passive wheels. While this design offers several advantages for reduced energy consumption, increased duration, and expanded coverage, dust caused by rotor downwash effects may reduce perception capabilities while driving [8]. Another class of land-air robots offers both active aerial and terrestrial motion [9], [11]. Active wheels are required in these systems to enhance ground moving performance [12], [14], [31].

This work was supported by the National High Technology Research and Development Program of China under Grant No. 2018YFE0204300, and the National Natural Science Foundation of China under Grant No. U1964203, and sponsored by Meituan and Tsinghua University-Didi Joint Research Center for Future Mobility.

<sup>1</sup>The School of Vehicle and Mobility, Tsinghua University, Beijing, P.R.China. xyzhang@tsinghua.edu.cn

<sup>2</sup>The School of Aviation, Inner Mongolia University of Technology, Hohhot, Inner Mongolia, P.R.China huangyuanhao.work@163.com

<sup>3</sup>The Department of Computer Science and Technology, Tsinghua University, Beijing, P.R.China. Kangyao Huang is the corresponding author. huangk22@mails.tsinghua.edu.cn

<sup>4</sup>Suzhou Automobile Research Institute, Tsinghua University, Suzhou, P.R.China. jindf@tsinghua.edu.cn



Fig. 1. A multi-modal deformable land-air robot.

The field of small land-air robotics has seen significant progress in recent years, due to highly integrated electronic components [15]. Although these robots balance athletic ability and agility, their small size limits them to short-term reconnaissance missions. In contrast, larger land-air robots can increase the duration of an operation and can carry heavier loads, but their large size can be difficult to maneuver in certain terrains [12]. Therefore, a land-air robots are difficult to have both strong flight ability and ground mobility. Previous studies have introduced deformable mechanisms to fold propeller to change size in the design of drones and land-air robot. However, most of these designs are based on small platforms [13], [16], since large deformations can limit actuator performance and restrict motion. As such, this study aims to develop a novel land-air robot with excellent ability to fly and drive. The proposed overall design conception in Section II can solve compatibility issues for multi-modal locomotive fusion with an hybrid land-air robot generally. Automatic deformable arms with fixed propellers offer stronger flight thrust than the same size robots. On this basis, the robot can become compact and move flexibly after folding its arms, and the it is also the first land-air robot with automatic folding arms. A series of experiments were conducted in buildings and fields as shown in Fig. 1. According to the motinve and passable experiments with rich scenarios and quantitative performance comparisons with related robots, we verify the robot’s capabilities of flying and driving. The primary technical contributions of this study can be summarized as follows:

- Proposed a generic overall design conception of land-

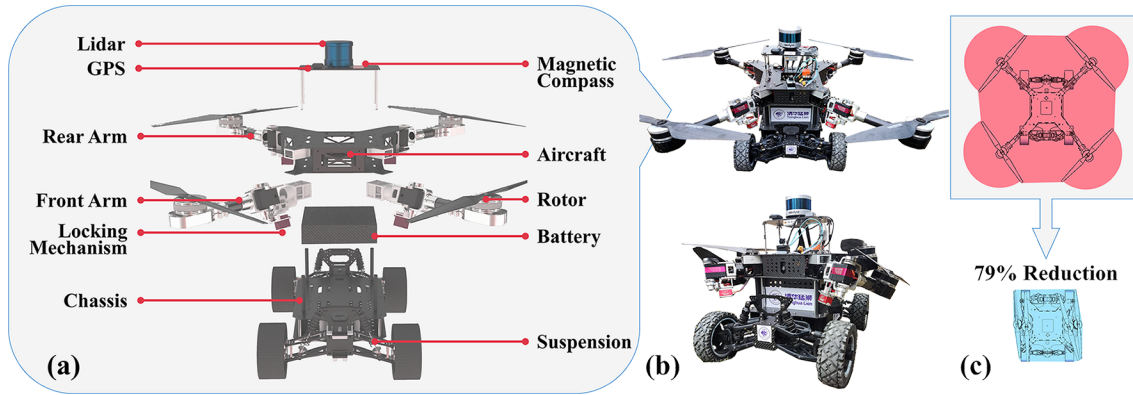


Fig. 2. The overall structure of the proposed robot, including the physical display and deformation advantages. (a) Key components, including flight, ground travel, and hardware elements. (b) Flight and driving modes. (c) The vertical projection area of the robot is reduced by 79 percent compared with the unfolded state.

air robot, considering the power settings, energy selection, lightweight design and deformable structure. The conception ensures the land-air robot's comprehensive movement ability.

- A land-air robot with automatic deformable arms is proposed for the first time. Combined with the introduced design conceptions, solving the land-air robots' compatibility issues between flying and driving modes. Larger propellers can generate greater thrust while reducing the plane projection area by 79 percent, which significantly improved passing capabilities.
- The proposed robot and mechanisms were verified in various simulated and practical field scenarios. The experiments and quantitative performance evaluation method provided strong evidences for their effectiveness and robustness.

The remainder of this paper is organized as follows. Section II introduces the design concept and corresponding analysis. Section III describes the detailed structure and deformable mechanism controls. Section IV provides the results of experiments and Section V concludes the paper. A video documenting experiments conducted as part of the study is available at [video](#).

## II. DESIGN CONCEPTS AND ANALYSIS

The design of the multi-modal land-air robot is not a simple combination, as multiple components (e.g., power and electronic systems) are shared to reduce the total weight to the extent possible. Despite this approach, moment of inertia of the robot is higher than normal land-air robots causes by weight and dispersed mass distribution. The compatibility problems of the motion speed characteristic requirements and controls present significant challenges [18]. In this section, we propose design metrics and concepts for power settings, energy selection, and the deformable structure of the land-air robot. The overall design and key parameters are shown in Fig. 2 and Table I.

### A. Overall Design

The robot configuration depends heavily on the requirements of specific tasks and corresponding environments.

TABLE I  
ROBOT SPECIFICATIONS

Width	Expanding	1250 mm
	Folding	585 mm
Depth	Expanding	1250 mm
	Folding	670 mm
Height	Body	552 mm
Weight	Total	24.62 kg
	Battery	5.74 kg
	Flight Module	7.61 kg
	Chassis	7.07 kg
	Payload	4.20 kg
Speed	Max Flying Speed	7.47 m/s
	Max Driving Speed	10.06 m/s
Flight Module	Flight Motor	5 Nm
	Kv Value	170
	Propeller	26 inch
	Steering Gear	8 Nm
Chassis	Kv Value	800
	Driving Motor	12 Nm
Battery	Lithium Battery	48 V-30 Ah
	Duration	21.6 min Flight Time

For example, most disaster rescue operations require robots to navigate through narrow passages, which places clear limitations on robot width. Thus, the dimensions of the robot were limited to within 70 centimeters in this study to allow for flexible motion and passage through narrow spaces for rapid searching. Despite these size restrictions, the robot is still expected to carry heavy equipment, including sensing devices, computing units, and actuators for improved situational awareness. As a typical example of this study, DJI ZENMUSE X7 and X5S are most commonly used camera sensors with stabilizer, which weight 449 gram and 461 gram [19] respectively. Similarly, ultra-wide view LiDAR sensors from Ouster weight around 500 gram for ordinary autonomous driving use [10]. Taking these configurations and load capacity demands into consideration, the maximum power and take-off weight can be estimated using existing techniques [20], [21]. Hereafter, we refer to the multi-copter flight evaluation strategy to optimize our approach, which provides a complete design and selection methodology for estimating and maximizing flight duration [22].

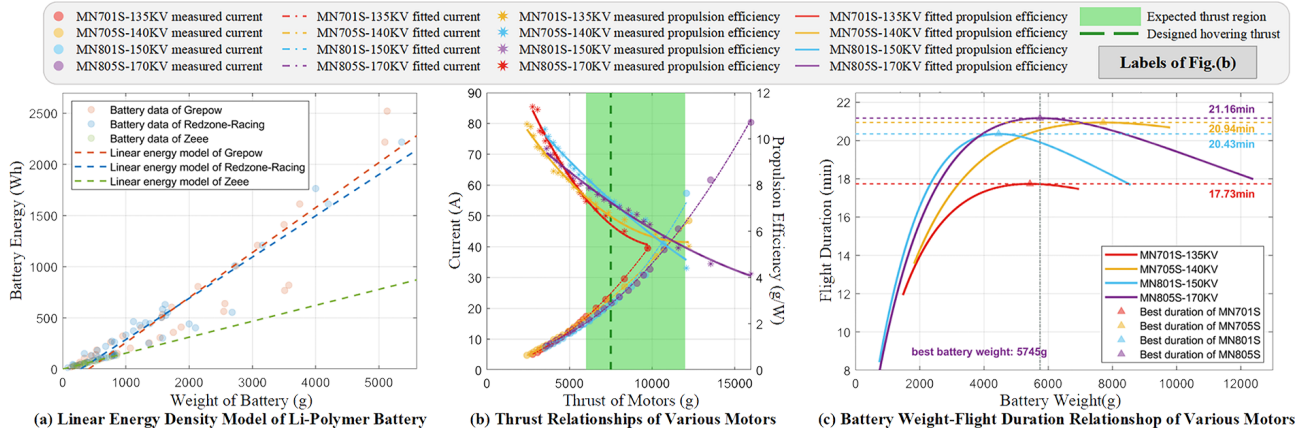


Fig. 3. Optimal flight duration analysis and power.

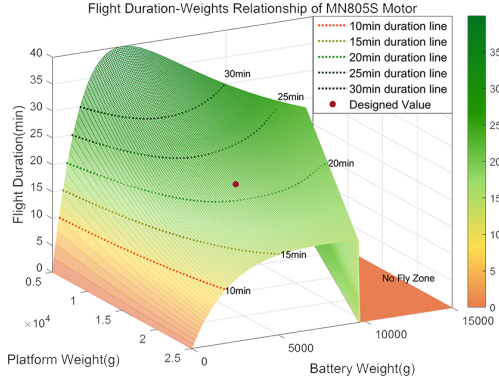


Fig. 4. Optimal flight duration for various robot weight configurations.

### B. Power Setting and Flight Duration Analysis

The trade-off between battery weight and flight duration is one of the most challenging aspects of the robot design process. We first evaluated flight duration using battery capacity and electrical current modeling for the motor/propeller system. The relationship between the Li-polymer battery's charge capacity and its mass is typically considered to be linear. We compared three different brands of batteries and obtained linear models using data fitting, as shown in Fig. 3(a). The maximum propeller size is fixed as 26 inch, we tentatively selected four power train configurations for use as assessment samples, with brushless motors (T-Motor) varying from 135~170 KV. Corresponding data combinations were then fitted into mappings, including variations in measured current and propulsion efficiency with thrust. All data are open-access and available on the T-Motor website at <https://uav-cn.tmotor.com/>. As shown in Fig. 3(b), the MN805S-170KV model can provide a large thrust range covering the expected region, with a relatively high propulsion efficiency that facilitates a higher energy efficiency for the entire power train.

The flight duration  $t$  can be estimated as follows:

$$t = \frac{wm}{\kappa VI + P}, P = P_{avionics} + P_{perception} + P_{deform}, \quad (1)$$

where  $w$  and  $m$  denote the energy density and mass of the battery, respectively,  $\kappa$  represents the number of motors in

the multi-copter (a constant),  $V$  is the nominal motor voltage,  $I$  is the instantaneous current, and  $P$  is the total power, consisting of power consumed by avionics systems, sensing devices, and deformations. Onboard power consumption can be calculated from the rated power and the mass of the robot. We set the calculated power rating to the output power when the robot hovering and was treated as a constant. Hovering thrust generated by the motors at rated power should be greater than or equal to the robot's weight. Thus, we can assume the hovering thrust is approximately equal to the combined weight of these modules:

$$T = W_r + W_b + W_d + W_a + W_p, \quad (2)$$

where  $W_r$ ,  $W_b$ ,  $W_d$ ,  $W_a$ , and  $W_p$  denote the weights of the robot frame, battery, deforming mechanical module, avionics devices, and payload, respectively. In some cases, increasing battery capacity can improve flight duration as more energy is provided. Flight time, however, may decrease if the battery is too heavy. The relationships between voltage, instantaneous current, and thrust (acquired by curve fitting) were used to develop a mapping relationship between flight duration and battery weight, as shown in Fig. 3(c). In this study, we strictly confined the robot's weight about 17 kg, excluding the battery. The results showed a robot with an MN805S-170KV power train and a  $\sim 5.7$  kg battery achieved the longest hovering duration ( $\sim 21$  minutes). Detailed relationships between the total robot weight and the battery weight utilizing T-Motor MN805S motors are provided in Fig. 4. The no-fly zone represents areas in which the robot cannot fly in a given configuration, due to excessive weight. In contrast, the lines of varying duration show weight configurations that can achieve flight. The proposed design is indicated by the red dot in the figure.

### C. Lightweight Design

Land-air robots are theoretically heavier than UAVs due to redundant actuators used for multi-modal motion and deformation. As such, achieving a lightweight design is extremely difficult with multi-modal robots, as there is always a compromise between weight and performance. This subsection describes the application of two frequently-used



lightweight optimization methods: light material selection and computer-aided structural optimization [23].

1) *Lightweight materials*: We first carefully screened the selected materials, using aerospace composites such as carbon fiber reinforced polymers (CFRPs) for the primary structure of the robot. However, some components that frequently withstand strong collisions and impacts require the use of metal. For example, the deformable structures and locking mechanisms adopted aluminium alloys (7xxx series) and high-strength steel. The differential casing and chassis cantilever were composed of a nylon material, which effectively guaranteed the strength of the fuselage structure. Each of these choices considered both the weight and strength.

2) *Computer-aided structural optimization*: The ANSYS finite-element and SolidWorks mechanical analysis tools were used to continuously reduce the total weight. The main body used CFRP and was designed as a box structure, which facilitated impact resistance and enhanced stiffness [24]. All components were designed with a honeycomb structure to reduce the weight. In the end, the arm deformation angle did not exceed 1.5 degree with the maximum thrust of the propellers, and the mass of the sheet was reduced by 27%.

### III. DEFORMABLE STRUCTURE DESIGN

Linkages [13] and putters [25] have successfully been used to actuate deformable structures in previous studies. However, redundant components create additional weight and can lead to more failures. As such, the proposed robot uses servos to drive the arms directly. Meanwhile, locking mechanisms and locking propeller motors are also highlights of the novel deformable structure.

#### A. Foldable Arms

A propeller's efficiency is significantly influenced by its diameter, as more power and thrust can be produced by larger propellers. For this reason, our robot uses 26-inch propellers to generate more thrust. However, propellers that are too large can cause issues for ground mobility, making it difficult to maneuver in confined spaces. In addition, a wide mass distribution can reduce the dynamic stability of the robot and induce vibrations [26]. As such, we propose a new type of oblique folding design in which the front arm is folded downward at an angle of 20 degrees and the rear arm is positioned horizontally to avoid physical interference between the front and rear arms. As the four arms rotate 135 degrees outward on the folding servo, the flight module unfolds and the platform enters flight mode, forming a square standard quad-rotor configuration.

Fig. 5(b) shows the deformable spatial motion path for the robot arm. The four arms form a circular path around the rotation axis of the deformable mechanism. Unlike in previous studies [13], proposed robot uses a unique motor for the fixed propeller, shown in Fig. 5(a) and Section III.C, to maintain the relative propeller angle in the same direction as the arm.

Fig. 5(c) shows the deformable mechanisms of the robot arms. As the motors begin to rotate, they generate tremendous amounts of torque at the dual-axis steering gears on

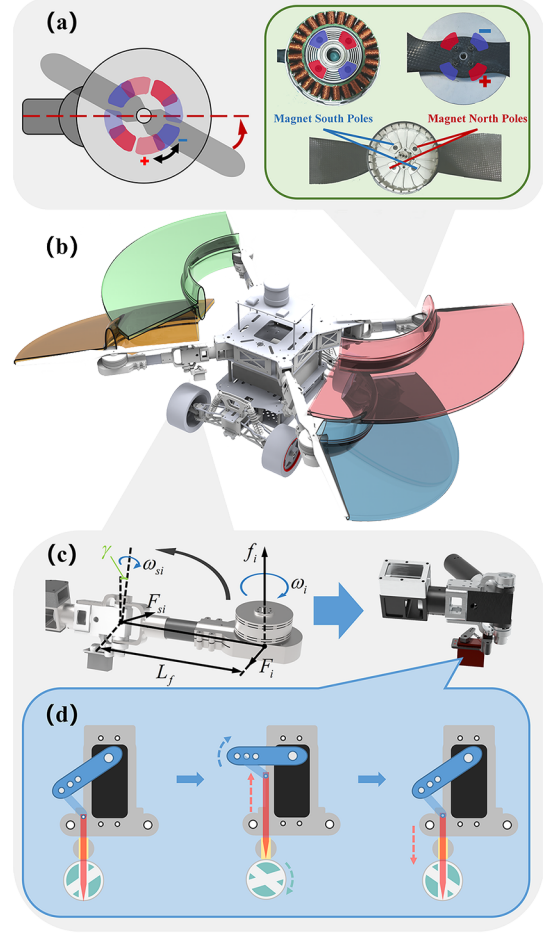


Fig. 5. A demonstration of the automated deformable structure. (a) A fixed propeller motor. (b) Motion paths in 3D space for the deformable structures. (c) A display of the deformable forearm. (d) The design and function of the locking mechanism.

the arms, as shown in Fig. 8. The Newton-Euler equation suggests a dynamic model for the quad-rotor aircraft can be expressed as:

$$M_b = J_b \dot{\omega}_b + \omega_b \times J_b \omega_b + M_g + M_d. \quad (3)$$

The synthesis of gyroscopic torque  $M_g$  and aerodynamic friction torque  $M_d$  can then be represented by:

$$M_g = \sum_{i=1}^4 \vec{\omega}_b \times J_b [0 \quad 0 \quad (-1)^{i+1} \Omega_i]^T, \quad (4)$$

$$M_d = \text{diag}(d_\phi, d_\theta, d_\psi) \dot{\zeta}, \quad (5)$$

where  $J_b = \text{diag}(d_\phi, d_\theta, d_\psi)$  is the moment of inertia for each rotor and  $d_\phi$ ,  $d_\theta$ , and  $d_\psi$  are the corresponding aerodynamic damping coefficients.

Complex deformable arms can affect the payload and reliability of land-air robots as each rotor is fixed to the main body of the robot by an independent arm. The propeller will then generate yaw forces during rotation, relying on the force generated by the steering gear to maintain the position of arms. Equations (3)-(5) suggest the moment of inertia for the arm can be expressed as:

$$J_{fi} = \frac{m_i}{12} L_{fi}^2 \times \cos(\gamma), \quad (6)$$



$$J_{ri} = \frac{m_i}{12} L_{ri}^2, \quad (7)$$

where  $m_i$  is the mass of the arm and  $J_i$  is the moment of inertia for the arm around the axis of the steering gear.  $L_{fi}$  and  $L_{ri}$  indicate the length of the front arms and the rear arms, respectively. The dynamic equation for the deformable arm is given by:

$$\text{diag}(m_i) \begin{bmatrix} \ddot{x} \\ \ddot{y} \\ \ddot{z} \end{bmatrix} = \begin{bmatrix} F_{xi} \\ F_{yi} \\ F_{zi} \end{bmatrix}, \quad (8)$$

where  $F_{xi}$ ,  $F_{yi}$ , and  $F_{zi}$  ( $i = 1 \dots 4$ ) are the decoupling forces along the x-axis, the y-axis, and the z-axis at the rotating shaft of each motor, respectively. The rotation matrix decouples these torques.

The reference coordinate is a global coordinate system. When the arm and the rotor rotate relative to the fuselage coordinate system, the inertia tensor for the arm will not rotate. This tensor can be expressed as:

$$J_{arm,i} = R_z(\theta_i) J_{arm} R_z(\theta_i)^T, \quad (9)$$

where  $R_z$  is the rotation matrix around the z-axis of the global coordinate system. The yaw angle is  $(\theta_i)$ ,  $i = (fl, fr, rl, rr)$ , and  $fl, fr, rl, rr$  demonstrate front left arm, front rear arm, rear left arm, and rear right arm, respectively. The moment of inertia for the motor does not change as it rotates around its z-axis.

### B. Locking Mechanism

A physical locking mechanism was included in the design to improve stability and ensure the safety of the robot. As shown in Fig. 5(d), the machine maintains 2 lock holes at key positions on the arms. The steering gear is then fixed on the rack and drives the auto-locking mechanism, while controlling pin movements by modifying draw bar rotation. These lock holes were denoted limiter-1 and limiter-2. Limiter-1 prevented the pin from deviating off the motion tracking course. Limiter-2 contained two key position holes, corresponding to the expanding and folding modes of the deformable arm. This pin could be accurately inserted into the holes by rotating the arm. This structure increased the operating safety of the platform in flight mode and effectively reduced the working pressure on the dual-axis steering gear.

### C. Fixed Propeller Motor

Unsecured propellers can cause collisions with the robot body during deformations. To address this issue, we designed a motor to ensure the propeller blades remained oriented in the direction of the arms. The motor included 2 south and 2 north magnetic poles added to the inner and outer rotors. As shown in Fig. 5(a), the propellers were fixed to the outer rotors, which relied on the magnets to quickly reset the propeller and keep it parallel to the arm at all times. This design prevented excessive energy loss during propeller rotation.

## IV. EXPERIMENTAL EVALUATION

The robustness and stability of the automated foldable arms were evaluated by simulations and experiments as part of the study. The resulting flexibility for land-air composite tasks was assessed using a 3D A\* search algorithm.

### A. Deformable Structure Experiments

This subsection describes the simulated validation of the proposed deformable structure. We measured and identified the mass, material, spatial distributions and others parameters in Tab. I for each structure. These data were used to construct a detailed co-simulation using ADAMS and MATLAB.

1) *Motion simulation*: Defined the front direction of the initial state of the robot as the two coordinates' x-direction, and established the global and robot coordinate systems with the right-hand rule. The robot then conducted three sets of experiments to obtain torques for the deformable arm structure. Figs. 6(a) and (b) show the deformable servos' torque produced during motion along the x and y axes. In both sets of experiments, the robot was tilted 15 degrees towards the x-axes and y-axes and moved along the directions. Fig. 6(c) shows torque variations while tracking a sinusoidal path, with trajectory and attitude changes shown in Fig. 7. Torques generated on the front arms were primarily concentrated at 3000 N·mm and torques on the rear arms were near 1000 N·mm. The torque on the deformable structure was also much smaller than the upper limit for the servos.

2) *Thrust simulation*: In the experiments, motor rotary speed was gradually increased from a standstill, reaching a maximum speed of 8000 rad/min. The torque generated on the deformable mechanism is shown in Fig. 8. A torque of

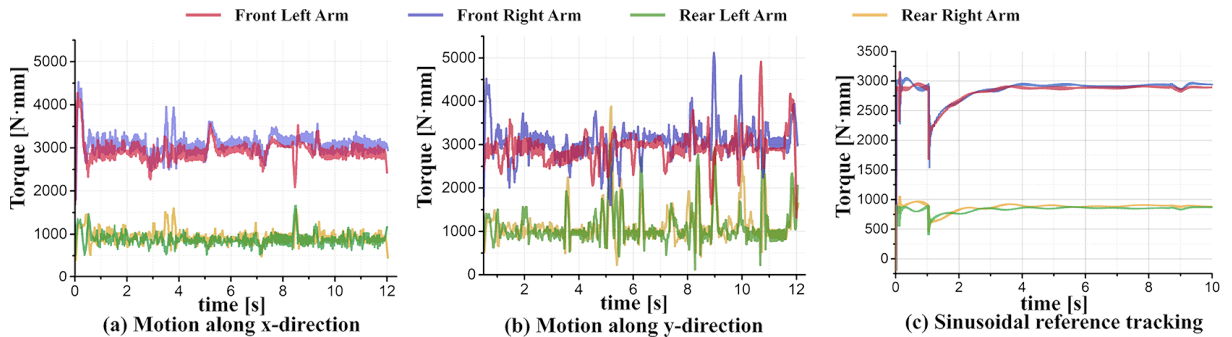


Fig. 6. Simulated torque on the deformable robot structure. (a) Accelerated motion in the x-direction. (b) Accelerated motion in the y-direction. (c) The robot performing a wave-like motion.

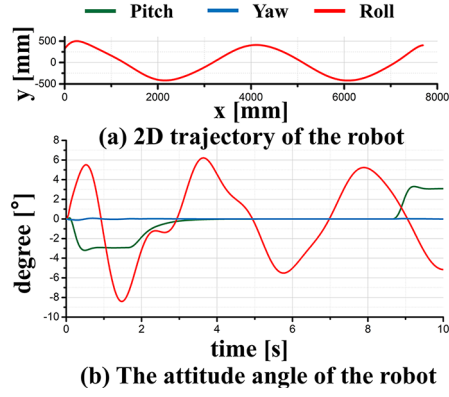


Fig. 7. Robot motion during sinusoidal reference tracking. (a) A top-view of the 2D robot trajectory. (b) The robot's attitude angle.

1000  $N \cdot mm$  was generated at rest, due to the inclination of the front arm. An increase in motor speed produced maximum torque on the front and rear arms of 6706  $N \cdot mm$  and 1711  $N \cdot mm$ , respectively, far from the upper limits of the design 7800  $N \cdot mm$ .

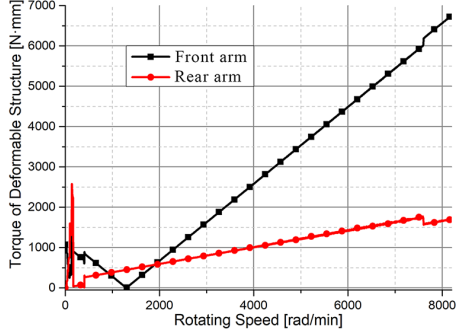


Fig. 8. The relationship between rotational speed and arm torque.

### B. Multi-modal Locomotion Planning

The flexibility of the robot was evaluated using a rescue scenario in an abandoned factory, which required the robot to search an optimal hybrid path to reach a specified target point. A DJI phantom 4 Pro was used to map the target area. The map was then rasterized, the obstacles were inflated, and the raw planned path was smoothed to satisfy the dynamic limits of flying and driving. As shown in Fig. 9, the robot originated from the center of the factory and attempted to reach three end points along the generation paths. The robot utilized multiple motion modes to fly over obstacles yet conserve energy, since the destinations were relatively isolated from the starting point. A simple rule-based algorithm was implemented based on 2D/3D A-star path planning [28], [29]. Energy consumption was considered in the process of heuristic algorithm design, so the robot would tend to drive on the ground rather than flying. As such, the robot demonstrated its adaptability and flexibility to various environments.

### C. Platform Tests

Experiments were conducted in both field and indoor environments under various scenarios, to verify performance.

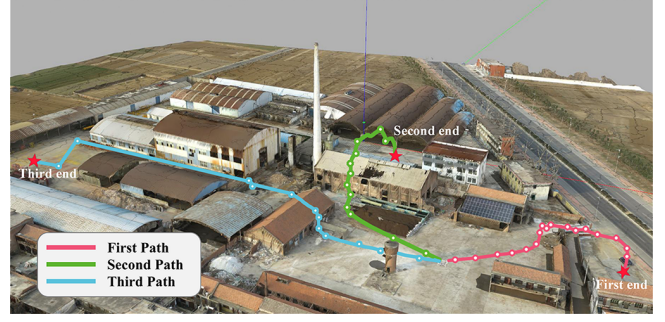


Fig. 9. The experiments demonstrate and verify the superiority and flexibility of the multi-modal robot in complex scenes.

The corresponding results are shown in Fig. 10 and a video is included in the link in Section I.

1) *Mode transition*: The first set of tests illustrated the transition process between flying and driving modes (the red and blue frames in Fig. 10). The robot only required 5 seconds to complete the deformation process. This practical experiment showed the robot could rapidly fold the arms and switch motion modes. The propellers could also be well positioned to avoid interference during transition.

2) *Driving in different scenarios*: In this experiment, the robot performed ground motion tests on flat roads, in unstructured scenes in the field, and in complex indoor environments. The robot exhibited a significant advantage in moving speed on structured paved roads, with a maximum speed reaching over 10  $m/s$ . Fig. 10 (see the yellow frame in Fig. 10) demonstrates highly flexible maneuvering on ground. In addition, the robot was tested on loose roads and in indoor human activity scenarios. It could easily pass through grasses, woods, and sandy ground, crossing a slope of more than  $30^\circ$  without slipping. However, it is restricted by its tire height, which made it challenging to overcome obstacles more than 100 mm in height (see the green frame in Fig. 10). The robot was also tested in warehouses, elevators, and dark corridors, in which it performed reliably and stably (see the orange frame in Fig. 10).

3) *Flying tests*: Flight tests were conducted outdoors, including takeoff, landing, acceleration, emergency braking, and path tracking (see the black frame in Fig. 10). During movement, the robot always maintained a normal posture and the desired control. In addition, the deformation mechanism operated stably without triggering an intervention from the locking mechanism. Some shaking did occur during take-off, due to ground spoilers. Meanwhile, we measured and estimated the robot's average power consumption during hovering and driving. The result shows that the power consumption of driving (2840 W) is 54.75 % lower than that of flying (6276 W).

### D. Evaluation and Comparison

In this subsection, we compare the proposed robot with other related works. The robot's size, duration, payload, and movement abilities are all critical manifestations of its performance [30]. Meanwhile, flight and ground movement capabilities need to be comprehensively evaluated. As such,

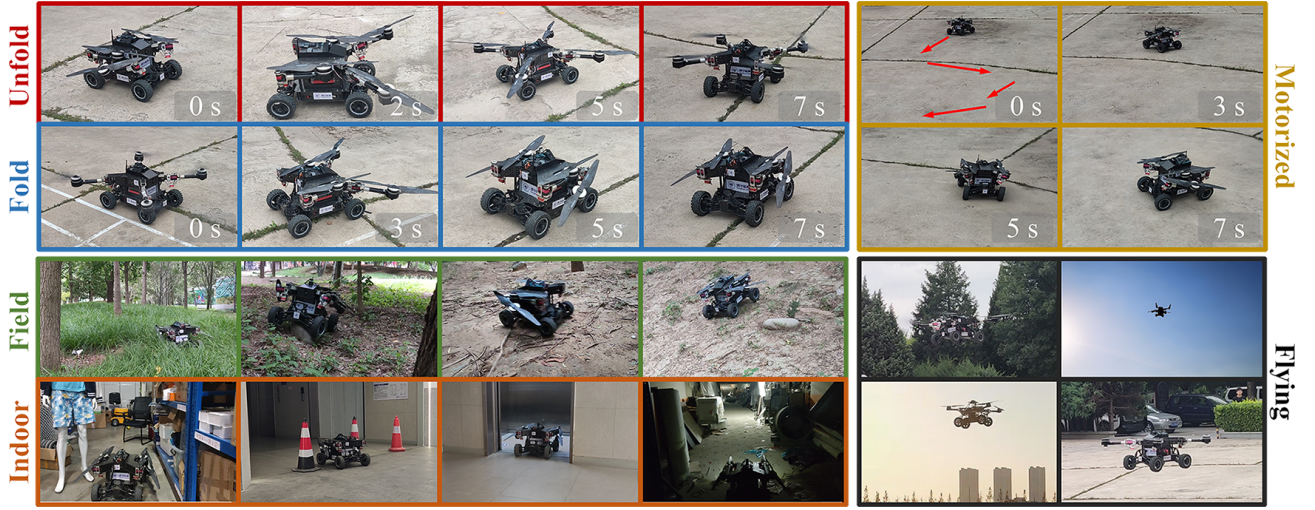


Fig. 10. Robot platform experiments.

we removed unit inconsistencies between all parameters and evaluated proposed robot with following indexes to obtain the comprehensive performance of the land-air robot [2], [6], [12], [31].

1) *Comprehensive flight ability*: Hovering flight duration  $t_f$ , payload  $p$ , and maximum tracking speed (air)  $v_f$  are critical indicators of the robot's index of flight capability  $F_e$ . They are also positively correlated with the robot's vertical projection area of flight state.  $w_i$  indicates the weight of the corresponding indicator set according to the task requirements, and this paper uses the same weight as 1. We use Min-Max normalization method to evaluate the comprehensive flight capability as follow

$$n(x) = \frac{x_i - x_{\min}}{x_{\max} - x_{\min}} \quad (10)$$

where  $x_i (i = 1 \dots n)$  express the parameters of robot  $i$ .  $x_{\max}$  and  $x_{\min}$  are the max and min values of the robots' same parameters.

$$F_e(t_f, p, v_f, S_{\text{land}}) = \sum_{i=t_f, p, v_f} w_i \cdot n(i) - w_s \cdot n(S_{\text{land}}) \quad (11)$$

2) *Comprehensive driving ability*: Similarly, the index of comprehensive ground performance  $G_e$  of the robot is evaluated by the ground driving mileage  $m_d$ , the obstacle-surmountable height  $h_o$ , and the maximum tracking speed (land)  $v_d$ .

$$G_e(m_d, h_i, v_d, S_{\text{air}}) = \sum_{i=m_d, h_i, v_d} w_i \cdot n(i) - w_s \cdot n(S_{\text{air}}) \quad (12)$$

3) *Modes switching time*: Modes switching time  $T_s$  express the time that robot switches from driving mode to flying mode or from flying mode to driving.

4) *Comprehensive duration*: Comprehensive duration in flying mode  $t_f$  and driving mode  $m_d$  are crucial for land-air robots' ability to undertake more productive tasks. And the duration is also strongly related to robots' weight  $G$ . Therefore, the land and air duration time  $D_e$  is comprehensively considered and used as a single evaluation index.

$$D_e(m_d, t_f) = \sum_{i=m_d, t_f} w_i \cdot n(i) - w_G \cdot n(G) \quad (13)$$

The results (Fig. 11) show that our robot got higher scores on  $F_e$  and  $G_e$ , thus that it has relatively comprehensive land and air capabilities. Meanwhile, the robot also got a slightly higher score on  $D_e$ . Although the mode switching speed of the robot is slow and the energy efficiency is slightly below than [2], [6], our design conception improve the robot's comprehensive abilities obviously. It should be noted that the comparison here is only a reference for the robot's capabilities. The parameters' weights in the method also need to be adjusted according to the specific task requirements. For example, [6] can perform more efficient and safe exploration

	Proposed Robot				Past work Tan Q, et al. [2]				Zhang R, et al. [6]				Qin Y, et al. [11]				Arash K, et al. [13]			
① to ③	21.62 min	4.2 kg	3.67 m/s		15.17 min	12 kg	3 m/s		9 min	0.5 kg	6 m/s		11.11 min	0.5 kg	5 m/s		8 min	1.2 kg	6 m/s	
④ to ⑥	18.21 km	110 mm	6.6 m/s		15.15 km	30 mm	2 m/s		5.81 km	100 mm	3 m/s		1.03 km	0 mm	0.6 m/s		5.40 km	155 mm	1 m/s	
⑦ to ⑨	24.62 kg	2.25 m <sup>2</sup>	0.49 m <sup>2</sup>		31.07 kg	5.55 m <sup>2</sup>	5.55 m <sup>2</sup>		0.85 kg	0.07 m <sup>2</sup>	0.07 m <sup>2</sup>		1.45 kg	0.51 m <sup>2</sup>	0.51 m <sup>2</sup>		5.1 kg	0.53 m <sup>2</sup>	0.53 m <sup>2</sup>	
	$F_e$	$G_e$	$T_s$	$D_e$	$F_e$	$G_e$	$T_s$	$D_e$	$F_e$	$G_e$	$T_s$	$D_e$	$F_e$	$G_e$	$T_s$	$D_e$	$F_e$	$G_e$	$T_s$	$D_e$
	1.46	2.31	$\approx 5$ s	0.43	0.53	0.24	$\approx 5$ s	0.35	1.07	1.33	$\approx 0$ s	0.35	0.48	-0.08	$\approx 3$ s	0.21	0.98	1.23	$\approx 1$ s	0.11

① Hovering Time ② Payload ③ Cruise Flying Speed ④ Driving Mileage ⑤ Obstacle Height ⑥ Cruise Driving Speed ⑦ Weight ⑧&⑨ Projection Area (Flying&driving)  
\*Notes: Unspecified payload is estimated by power and weight, obstacle-overcoming height by the wheel's radius, cruise driving speed by hovering time and energy efficiency.

Fig. 11. Comprehensive performance quantitative evaluation of proposed robot, past work and typical land-air robot.



in narrow and complex scenarios. When evaluating such robots, we can increase the weights of flight and size. The evaluative method can also introduce quantitative indicators such as climbing performance and security.

## V. CONCLUSION

This study proposed a multi-modal land-air robot with automatic deformable arms for the first time, with the design conception which solving the compatibility issues for the hybrid land-air robot. By estimated and calculated the powers and energy, the robot got a suitable battery and power settings. Meanwhile, a simple yet reliable foldable structure was used to significantly expand the space for a flight mechanism and increase the thrust. This approach also reduced the size of the driving mode and allowed the platform to traverse narrow corridors. The robot was tested in cement pavement, field and indoor, we knew that the driving consumption is 54.75 % lower than flying consumption. Compared with other land-air robots by proposed evaluation methods, our robot offers better comprehensive for flying ability, as well as improved roadway driving capabilities. The robot had a good balance of flight and driving comprehensive capabilities.

## REFERENCES

- [1] M. Rafeeq, S. F. Toha, S. Ahmad, and M. A. Razib, "Locomotion Strategies for Amphibious Robots-A Review," *IEEE Access*, vol. 9, pp. 26 323–26 342, 2021.
- [2] Y. Qin, Y. Li, X. Wei, and F. Zhang, "Hybrid aerial-ground locomotion with a single passive wheel," in *2020 IEEE/RSJ International Conference on Intelligent Robots and Systems (IROS)*. IEEE, 2020, pp. 1371–1376.
- [3] N. Meiri and D. Zarrouk, "Flying star, a hybrid crawling and flying sprawl tuned robot," in *2019 International Conference on Robotics and Automation (ICRA)*. IEEE, 2019, pp. 5302–5308.
- [4] A. Kalantari and M. Spenko, "Design and experimental validation of HyTAQ, a Hybrid Terrestrial and Aerial Quadrotor," *Proceedings - IEEE International Conference on Robotics and Automation*, pp. 4445–4450, 2013.
- [5] C. J. Dudley, A. C. Woods, and K. K. Leang, "A micro spherical rolling and flying robot," *IEEE International Conference on Intelligent Robots and Systems*, vol. 2015-Decem, pp. 5863–5869, 2015.
- [6] R. Zhang, Y. Wu, L. Zhang, C. Xu, and F. Gao, "Autonomous and adaptive navigation for terrestrial-aerial bimodal vehicles," *IEEE Robotics and Automation Letters*, vol. 7, no. 2, pp. 3008–3015, 2022.
- [7] X. Zhang, J. Huang, Y. Huang, K. Huang, L. Yang, Y. Han, L. Wang, H. Liu, J. Luo, and J. Li, "Intelligent amphibious ground-aerial vehicles: State of the art technology for future transportation," *IEEE Transactions on Intelligent Vehicles*, 2022.
- [8] S. Wen, J. Han, Z. Ning, Y. Lan, X. Yin, J. Zhang, and Y. Ge, "Numerical analysis and validation of spray distributions disturbed by quad-rotor drone wake at different flight speeds," *Computers and Electronics in Agriculture*, vol. 166, p. 105036, 2019.
- [9] P. Ratsamee, P. Kriengkamol, T. Arai, K. Kamiyama, Y. Mae, K. Kiyokawa, T. Mashita, Y. Uranishi, and H. Takemura, "A hybrid flying and walking robot for steel bridge inspection," *SSRR 2016 - International Symposium on Safety, Security and Rescue Robotics*, pp. 62–67, 2016.
- [10] Ouster, "High-performance digital lidar solutions," 2022. [Online]. Available: <https://ouster.com/>
- [11] A. Kalantari, T. Touma, L. Kim, R. Jitosh, K. Strickland, B. T. Lopez, and A. A. Agha-Mohammadi, "Drivocopter: A concept Hybrid Aerial/Ground vehicle for long-endurance mobility," *IEEE Aerospace Conference Proceedings*, 2020.
- [12] Q. Tan, X. Zhang, H. Liu, S. Jiao, M. Zhou, and J. Li, "Multimodal dynamics analysis and control for amphibious fly-drive vehicle," *IEEE/ASME Transactions on Mechatronics*, vol. 26, no. 2, pp. 621–632, 2021.
- [13] J. Hu, Y. Liang, and X. Diao, "A flying-insect-inspired hybrid robot for disaster exploration," *2017 IEEE International Conference on Robotics and Biomimetics, ROBIO 2017*, vol. 2018-Janua, pp. 270–275, 2018.
- [14] A. Sharif, S. Choi, and H. Roth, "A new algorithm for autonomous outdoor navigation of robots that can fly and drive," *ACM International Conference Proceeding Series*, vol. Part F1476, pp. 141–145, 2019.
- [15] J. James and S. Fuller, "A high-voltage power electronics unit for flying insect robots that can modulate wing thrust," in *2021 IEEE International Conference on Robotics and Automation (ICRA)*. IEEE, 2021, pp. 7212–7218.
- [16] D. Falanga, K. Kleber, S. Mintchev, D. Floreano, and D. Scaramuzza, "The foldable drone: A morphing quadrotor that can squeeze and fly," *IEEE Robotics and Automation Letters*, vol. 4, no. 2, pp. 209–216, 2018.
- [17] H. Wang, J. Shi, J. Wang, H. Wang, Y. Feng, and Y. You, "Design and modeling of a novel transformable land/air robot," *International Journal of Aerospace Engineering*, vol. 2019, 2019.
- [18] W. Xie, D. Cabecinhas, R. Cunha, and C. Silvestre, "Adaptive backstepping control of a quadcopter with uncertain vehicle mass, moment of inertia, and disturbances," *IEEE Transactions on Industrial Electronics*, vol. 69, no. 1, pp. 549–559, 2021.
- [19] DJI, "DJI Online Store," 2022. [Online]. Available: [www.dji.com](http://www.dji.com)
- [20] D. Shi, X. Dai, X. Zhang, and Q. Quan, "A practical performance evaluation method for electric multicopters," *IEEE/ASME Transactions on Mechatronics*, vol. 22, no. 3, pp. 1337–1348, 2017.
- [21] X. Dai, Q. Quan, J. Ren, and K.-Y. Cai, "An analytical design-optimization method for electric propulsion systems of multicopter uavs with desired hovering endurance," *IEEE/ASME Transactions on Mechatronics*, vol. 24, no. 1, pp. 228–239, 2019.
- [22] X. He, J. R. Bourne, J. A. Steiner, C. Mortensen, K. C. Hoffman, C. J. Dudley, B. Rogers, D. M. Crokek, and K. K. Leang, "Autonomous Chemical-Sensing Aerial Robot for Urban/Suburban Environmental Monitoring," *IEEE Systems Journal*, vol. 13, no. 3, pp. 3524–3535, 2019.
- [23] L. Zhu, N. Li, and P. Childs, "Light-weighting in aerospace component and system design," *Propulsion and Power Research*, vol. 7, no. 2, pp. 103–119, 2018.
- [24] Y. Zhu, Z. Guo, T. Li, and M. Wang, "Implementation and performance assessment of triphibious robot," in *2019 IEEE International Conference on Mechatronics and Automation (ICMA)*. IEEE, 2019, pp. 1514–1519.
- [25] Y. Huang, R. Meng, J. Yu, Z. Zhao, and X. Zhang, "Practical obstacle-overcoming robot with a heterogeneous sensing system: Design and experiments," *Machines*, vol. 10, no. 5, 2022. [Online]. Available: <https://www.mdpi.com/2075-1702/10/5/289>
- [26] W. Saab, W. S. Rone, and P. Ben-Tzvi, "Robotic tails: a state-of-the-art review," *Robotica*, vol. 36, no. 9, pp. 1263–1277, 2018.
- [27] R. Zufferey, A. O. Ancel, C. Raposo, S. F. Armanini, A. Farinha, R. Siddall, I. Berasaluce, H. Zhu, and M. Kovac, "Sailmav: Design and implementation of a novel multi-modal flying sailing robot," *IEEE Robotics and Automation Letters*, vol. 4, no. 3, pp. 2894–2901, 2019.
- [28] F. Duchón, A. Babinec, M. Kajan, P. Beño, M. Florek, T. Fico, and L. Jurišica, "Path planning with modified a star algorithm for a mobile robot," *Procedia Engineering*, vol. 96, pp. 59–69, 2014.
- [29] L. Yang, J. Qi, J. Xiao, and X. Yong, "A literature review of uav 3d path planning," in *Proceeding of the 11th World Congress on Intelligent Control and Automation*. IEEE, 2014, pp. 2376–2381.
- [30] C. Nie, X. P. Corcho, and M. Spenko, "Robots on the move: Versatility and complexity in mobile robot locomotion," *IEEE Robotics & Automation Magazine*, vol. 20, no. 4, pp. 72–82, 2013.
- [31] A. Kalantari, T. Touma, L. Kim, R. Jitosh, K. Strickland, B. T. Lopez, and A.-A. Agha-Mohammadi, "Drivocopter: A concept hybrid aerial/ground vehicle for long-endurance mobility," in *2020 IEEE Aerospace Conference*. IEEE, 2020, pp. 1–10.